ACS APPLIED MATERIALS & INTERFACES

Research Article

www.acsami.org

In Situ Raman Spectroscopic Study of Al-Infiltrated Spider Dragline Silk under Tensile Deformation

Seung-Mo Lee,*[,†,‡] Eckhard Pippel,[§] Oussama Moutanabbir,[∥] Jae-Hyun Kim,[†,‡] Hak-Joo Lee,[†] and Mato Knez[⊥,#]

[†]Department of Nanomechanics, Nano-Mechanical Systems Research Division, Korea Institute of Machinery & Materials (KIMM), 156 Gajungbukno, Yuseong-gu, Daejeon, 305-343, Korea

[‡]Nano Mechatronics, University of Science and Technology (UST), 217 Gajeong-ro, Yuseong-gu, Daejeon 305-333, South Korea

[§]Max Planck Institute of Microstructure Physics, Weinberg 2, D-06120 Halle, Germany

[∥]Department of Engineering Physics, Ecole Polytechnique de Montreal, C.P. 6079, Succ. Centre-Ville, Montréal, Québec H3C 3A7 Canada

[⊥]CIC nanoGUNE Consolider, Tolosa Hiribidea 76, E-20018 Donostia - San Sebastian, Spain

[#]IKERBASQUE, Basque Foundation for Science, Alameda Urquijo 36-5, E-48011 Bilbao, Spain

ABSTRACT: Natural materials consisting of protein structures impregnated with a tiny amount of metals often exhibit impressive mechanical behavior, which represents a new design paradigm for the development of biomimetic materials. Here, we produced Al-infiltrated silks by applying a modified Al_2O_3 atomic layer deposition process to the dragline silk of the *Nephila pilipes* spider, which showed unusual mechanical properties. The deformation behavior of the molecular structure of the Al-infiltrated silk was investigated by performing in situ Raman spectroscopy, where Raman shifts were measured concurrently with macroscopic mechanical deformations. For identifying the role of the infiltrated Al atoms, the study was performed in parallel with untreated silk, and the results were compared. Our experimental results revealed that superior mechanical properties of the Al-infiltrated silk are likely to be caused by the alterations of the sizes of the β-sheet crystals and their distribution.

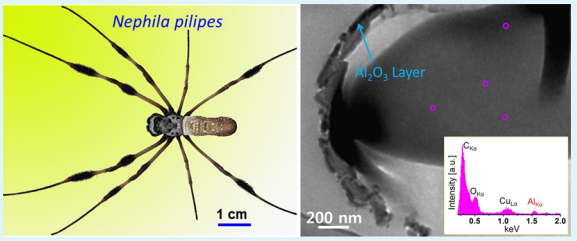

KEYWORDS: *metal-impregnated biological materials, mechanical properties, spider dragline silk, atomic layer deposition, vapor phase infiltration*

INTRODUCTION

Genghis Khan, who approximately 800 years ago conquered most of the Eurasian continents is mostly remembered as an emperor who wanted to create the largest empire in the world with a highly efficient army. However, there is also an interesting story related to material science associated with Genghis Khan. This story claims that his warriors were protected from enemy arrows by special leather garments, which were interwoven with one of the strongest materials known at that time, silk.[1,2] Spider dragline silk from major-ampullate silk glands outperforms almost any man-made material in its combination of tensile strength and extensibility (so-called, extreme toughness).[2−4] These remarkable mechanical properties of the dragline silk aroused considerable interest by scientists, with research focusing on elucidation the relationship between molecular conformation and mechanical properties of the dragline silk[5] or artificial silk production.[6] However, surprisingly, approaches to improve or tune the mechanical properties of the native or produced spider silk themselves through chemical treatments have rarely been undertaken.[7,8] The focus has rather been on harvesting[9] or converting spider silks into fabric form[12] or reinforcing *Bombyx mori* silk with certain additives like carbon nanotubes[10] or nanoparticles.[11]

Recently, we discovered that applying metal oxide atomic layer deposition (ALD) processes to the dragline silk of *Araneus* spiders results in drastic improvement of mechanical properties induced by the metal infiltration into the protein structures of the silk rather than coating.[13] We also learned that nature already provides prodigious role models associated with our results. Namely, some metal ions endow certain biological materials with a number of intriguing mechanical properties such as, high hardness/stiffness, self-repairing, etc. Removing the metal from those materials often results in sudden loss of such properties.[14−17] Further research revealed that the metal infiltration phenomenon induced by the ALD process can be also realized with further biomaterials and even the chemically inert polymer, polytetrafluorethylene (PTFE).[18−21] Those experiments imply that the ALD process is indeed one of the promising means to endow certain materials with exceptional

Received: June 27, 2014
Accepted: September 9, 2014
Published: September 9, 2014

chemical and physical properties. However, the role of the infiltrated inorganics and the origin of the associated mechanical property improvement after metal-infiltration appears to be different from natural materials and requires more in-depth understanding. Compared to the native spider silk, the metal-infiltrated spider dragline silk unusually showed a nearly 2-fold increase in both strength and extensibility. However, the molecular alteration of those silks, which is supposedly the origin of such unusual tensile behavior, remains less understood. In this work, we applied an Al_2O_3 ALD process commonly resulting in tens of nanometer thickness to the dragline silk of a *Nephila pilipes* spider, which has in general higher extensibility compared to that of an *Araneus* spider.[22] Initially, we compared the macroscopic deformation behavior of the *Nephila* spider dragline silk before and after ALD processing using an uniaxial tensile test. The results showed that metal infiltration phenomena similar to those observed from the *Araneus* silks occur with the *Nephila* spider silk as well. The alterations of those silks on the molecular level were examined in situ, combining a uniaxial tensile test and Raman spectroscopy.

EXPERIMENTAL SECTION

Dragline Silk Preparation. From fully awake *Nephila pilipes* spiders raised in the laboratory on a diet of flies and crickets, we obtained dragline silk (major ampullate silk) using a forced silking method. Using pins, we immobilized the spider on a Styrofoam block. First, under the optical microscope, we observed the silk glands. Then, the dragline silk was wound on a steel wire spool with a reeling speed of ∼20 mm/s under ambient conditions (∼20 °C and 30% relative humidity). All measurements and characterizations were performed within 30 d.

Atomic Layer Deposition. The prepared spider dragline silks were placed into an ALD reactor (Savannah S100, Cambridge Nanotech Inc.) and dried at 70 °C for 5 min in vacuum (1×10^{-2} Torr) with a steady Ar gas stream (20 sccm). Trimethylaluminum (TMA, $(CH_3)_3Al$, purchased from Sigma-Aldrich) and purified water were used as sources for Al and oxygen, respectively. Each cycle was composed of a pulse, exposure, and purge sequence for each precursor. The TMA vapor was injected into the ALD chamber during a 0.1 s pulse. Subsequently, the substrate was exposed to the TMA vapor for 30 s (exposure). The excess TMA was purged from the ALD chamber for 40 s (purge). In the same manner, the pulse (1.0 s)/exposure (30 s)/purge (40 s) processes of water were repeated. The described sequence was repeated 500 times. The growth rate of Al_2O_3 ALD on SiO_2 substrate (control sample) was measured to be around 1 Å/cycle.

Scanning Electron Microscopy. The morphology and the diameters of the dragline silk before and after the Al_2O_3 ALD process were examined by JEOL JSM-6340F SEM at 10 kV after deposition of Pt with thickness of ∼3 nm. The diameters of the silks were measured to be ∼4.8 μm. The measurements were repeated several times, and the measured diameters were averaged.

Tensile Test. In advance of the in situ Raman spectroscopy analysis of the silks, uniaxial tensile tests were performed. For the tests, the prepared silk samples (monofilament) were mounted on a thick paper jig having punched holes with a diameter of 2 cm. The paper jigs were used to facilitate alignment and clamping of the specimens during the tensile test. With the support of the jigs, the silk was maintained in a straight position during clamping. Furthermore, the jigs allowed for easy cutting through the cutting line so that silk specimen and paper jigs were not simultaneously loaded during the actual test. Epoxy resin was used as glue to fix the silk to the edges of the jig. Prior to the measurement, under an optical microscope (Leitz Aristomet) and a magnifying glass (×10), the quality of all samples was carefully examined: a proper fixation with glue and any surface damage of the silk. Because the samples might have been unintentionally damaged during handling and transport, one had to pay careful attention. At this stage, samples with poor fixation or surface damage were excluded. The tensile test was performed at ambient conditions on a ZWICK 1445 tensile test machine with 10 N HBM load cell and controlled with a personal computer having automated testing software. The extension rate was 5% of the initial length per minute (1 mm/min). The fiber was extended until fracture occurred. For precise results, over 10 samples were prepared and measured. Most of the samples showed similar tensile behavior. Force (mN)−strain (%) data for each specimen were exported from the software of the machine, and subsequently the data were rescaled into the engineering stress (σ)−engineering strain (ε) using ORIGIN8.0.

Transmission Electron Microscopy and Energy-Dispersive X-ray Spectroscopy. To prepare cross-sectional samples of the silk for TEM and EDX analysis, the used spools wound by the silk were fixated with 3% glutaraldehyde (Sigma, Taufkirchen, Germany) in 0.1 M sodium cacodylate buffer (SCB, pH 7.2) for 2 h at room temperature, rinsed with SCB, dehydrated in a graded ethanol series, infiltrated with epoxy resin, and polymerized at 70 °C for 24 h. Ultrathin sections (90 nm) were made with an Ultracut R ultramicrotome (Leica, Wetzlar, Germany) and transferred to copper grids, coated with a carbon film. TEM and EDX examinations (imaging, line scans, and point analyses) were carried out with a FEI TITAN 80−300 microscope (300 kV) in scanning transmission mode.

Wide-Angle X-ray Diffraction. Around 500 native and Al-infiltrated silk filaments were glued on a piece of separated silicon wafers (2 cm × 2 cm) with a double-faced soft tap. Wide-angle X-ray diffractometer (Philips X'Pert MRD with 50 kV, 30 mA) with Ni-filtered Cu Kα (λ = 1.5421 Å) radiation was used to obtain the diffraction profiles, which were measured in 2θ scans across the fiber diameter. The measured angular range and step size was $5° < 2\theta < 25°$ and 0.1°, respectively. The applied exposure time was 90 s/step. For each measurement, at least three identical samples were prepared, and the measurements were repeated at least five times with each sample. Most of the spectra showed similar shapes, peak locations, and intensities. One representative spectrum was selected for demonstration. All graphical tasks were performed with ORIGIN 8.0.

Raman Investigation under Strain Control. In situ micro-Raman measurements were carried out at room temperature in backscattering geometry with a LabRam HR800 UV spectrometer with the following laser lines: 633 nm He−Ne laser, 514 and 488 nm Ar ion laser, and 325 nm He−Cd laser. To avoid local heating effects, the laser power density was kept below 100 $\mu W/\mu m^2$. Data obtained from different objectives corresponding to different laser spot diameters on the sample at a fixed laser power confirmed the absence of the heating effects. Using the objective (×100, NA = 1.4), the laser beam focused on the center of the monofilament of the silks, as shown in Figure 3. The backscattered Raman light is diffracted by a 1800 g/mm grating and detected by a highly sensitive charged coupled device camera. The spectral distance between adjacent channels was ∼0.5 cm^{-1}. The spectra measured with 488 and 514 nm lasers show a strong fluorescence background, which limits the extraction of meaningful data. In this work, only data recorded with the 633 nm laser are presented. The Raman spectrometer equipped with a home-built uniaxial tensile tester allowed the spectra to be recorded under macroscopic strain. Similar types of paper jigs having punched holes with a diameter of 1 cm were employed. The monofilament of the silk was glued on the paper jig, which was tightly mounted on tensile tester with screw grips. After the edge of the jig was cut, the monofilaments were controlled to be stretched to failure in steps of 1−3% strain. The spectra of both the stress−strain curve of a single filament of the native dragline silk (SS/N) and stress and strain of the ALD-processed spider silk (SS/Al) were recorded in wavenumber intervals of 1000−1800 and 3000−3600 cm^{-1} under the extended range configuration, respectively. For each deformation step, the spectrum was recorded for 600 s, which was required to obtain enough signal-to-noise ratio to perform data analysis. Because our Raman measurements were performed under stepwise extension of the silk, one may wonder whether the stress-relaxation of the silk would influence the Raman shifts. However, it has been reported that although the instantaneous band shifts by application of load occur, there are no subsequent

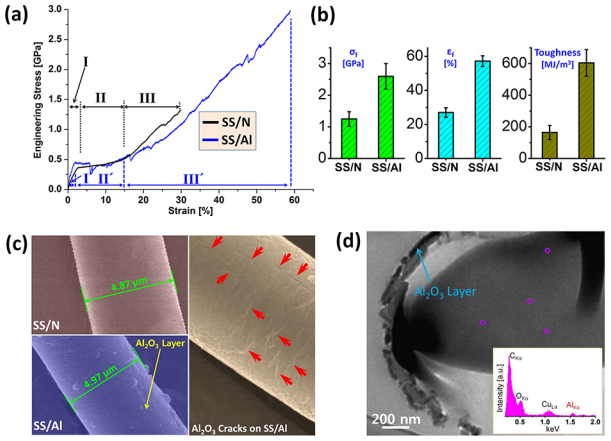

Figure 1. Mechanical properties of the *Nephila pilipes* spider dragline silk before/after Al_2O_3 ALD treatment and element analysis. (a) Typical stress−strain curves of the native (SS/N) and Al-infiltrated (SS/Al) spider dragline silk. (b) Failure strength, failure strain and toughness of SS/N and SS/Al, respectively. (c) SEM images of SS/N and SS/Al. The red arrows indicate cracks of Al_2O_3 layer induced by cooling from deposition temperature (70 °C) to room temperature. (d) TEM image of a cross sectioned SS/Al sample. (inset) One of EDX point analysis results measured at the positions marked with pink circles in the TEM image. The intensities of the Al signal were observed to be generally weak but well above background intensity.

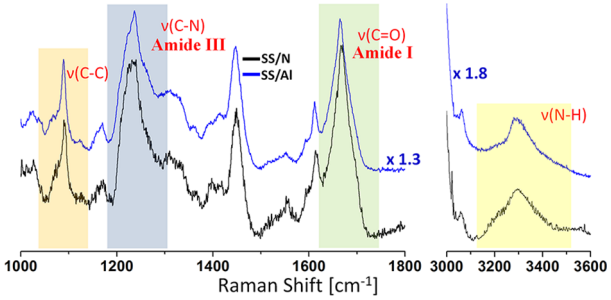

Figure 2. Comparison of representative Raman spectra for single filaments of SS/N and SS/Al samples measured before mechanical deformation (ε = 0).

significant changes in the shifts with time (up to 8000 s).[23] More than 10 sets of samples were prepared identically and measured under the same conditions to ensure data reliability. All graphic works including data rescaling were performed with ORIGIN 8.0.

RESULTS AND DISCUSSION

Mechanical Properties of Al-Infiltrated Spider Silk. As precursor pairs for the ALD process, TMA, a highly reactive Al source, and water vapor were selected for the treatment of *Nephila pilipes* dragline silk. The dragline silk itself was extracted by the forced silking technique.[24] The SS/N showed similar trends and material properties (e.g., yield stress/strain, breaking stress/strain) to those reported in literature.[25] An ALD process with 500 cycles (~50 nm nominal thickness of Al_2O_3) applied to the *Nephila* dragline silk gave rise to a drastic improvement of mechanical properties in analogy to the earlier observation from the *Araneus* spider silk. Figure 1a,b shows that both the failure SS/Al increase by the factor of 2 as compared to the native nontreated silk (SS/N). In addition, the breaking energy increased nearly 3-fold. Given that the coefficients of thermal expansions (CTEs) of dragline silk and Al_2O_3 are ~1060 ppm/K[26] and ~4.2 ppm/K,[27] respectively, it is trivial

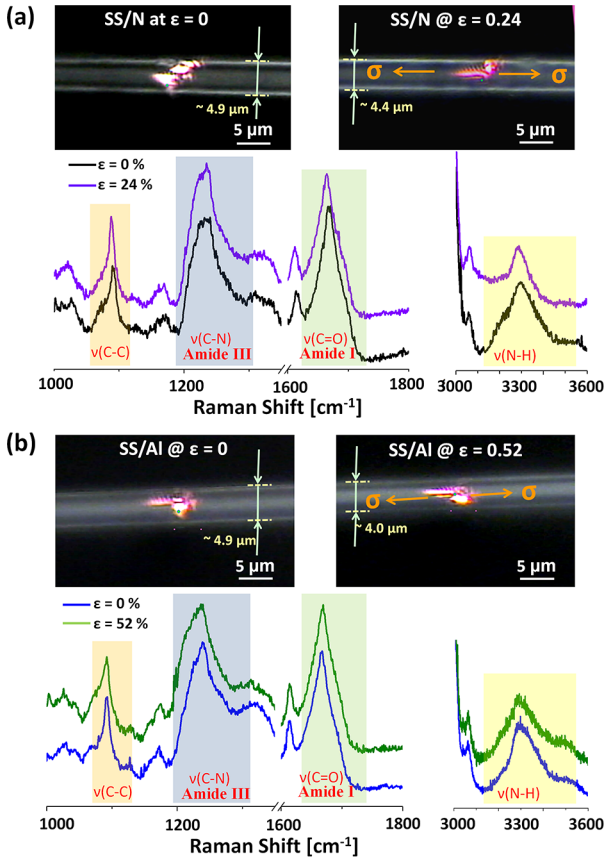

Figure 3. Comparison of representative Raman band shifts of (a) SS/N and (b) SS/Al upon mechanical deformation. (insets) Optical microscope images showing the focused laser beam (633 nm).

that the large CTE mismatch and the resultant compressive thermal stress lead to buckling and cracking of the Al_2O_3 film upon cooling from deposition temperature (70 °C) to room temperature (Figure 1c). Furthermore, because fracture stress and strain of Al_2O_3 film with thickness of ~50 nm in compressive load are in the range of 0.7 GPa and 0.4%, respectively,[28] the Al_2O_3 layer seemed to have little effect on the mechanical properties of core/shell structure composed of Al_2O_3 layer and silk. Consequently, the infiltrated aluminum (Figure 1d) is thought to obviously change the protein structure of the native silk seriously, which is further validated from the following *in situ* Raman spectroscopic studies.

Spider silk is a hierarchically structured semicrystalline biopolymer containing stiff/strong crystals and flexible amorphous regions. The crystals (β-pleated sheets) have varying sizes and are composed of amino acid groups (predominantly alanine, glycine, glutamine, etc.) arranged in an accordion-like fashion.[29−31] The amorphous regions contain protein chains with about 15 amino acid-long chains on the average.[32] In addition, main linkages between amino acids within crystals and amorphous regions are hydrogen bonds, which are known to play a key role in the formation and stabilization of secondary structures of the proteins.[33] Particularly, interpeptide hydrogen bonds stabilize secondary structures such as α-helix and β-sheet conformations.

In Situ Raman Study. Raman spectroscopy is a well-established technique for evaluating molecular structures of the dragline silks and appears most useful for examining molecular deformation mechanisms of the silks during mechanical

dx.doi.org/10.1021/am5041797 | ACS Appl. Mater. Interfaces 2014, 6, 16827−16834

loading.[22,23] The wavenumbers ($\Delta\nu$) of the Raman bands tend to shift under the action of applied stress and strain. The amount of shift allows insight into the molecular change of the individual bonds in the dragline silks. As depicted in Figure 2, the infiltrated Al appears strongly influential on the protein structure of the dragline silk. Notably, while the ν(C−C) skeletal stretching mode revealed nearly unchanged, the main differences between the native and the Al-infiltrated silks were observed in the region of amide **I** (at 1668 cm^{-1}, ν(C═O), β-sheet), amide **III** (at 1240 cm^{-1}, ν(C−N), β-sheet), and amide **A** (ν(N−H) stretching vibrational modes).[34] Taking into account that these modes are known to depend on the hydrogen bonding states of the peptide bonds, the infiltrated Al atoms are believed to be affecting the hydrogen bonds. Presumably the Al atoms form coordinate bonds during the multiple pulsing of highly reactive TMA and water precursors.

Upon mechanical deformation of the silk fiber, the covalent bonds within the protein structures of the silk are stressed. This leads to an alignment of the molecules along the direction of tension. The deformation of the oriented molecules in both the crystalline and amorphous regions gives rise to a change in bond lengths and bond angles. This induces a change in the corresponding force constants, which can be monitored by measuring the related Raman shifts. Single fibers of both native and Al-infiltrated silks were deformed under controlled strain to failure. At the same time, variances in Raman bands related to amide **I**, amide **III**, amide **A** (ν(N−H) stretching), and ν(C−C) skeletal stretching modes were traced to capture the dissimilarities in the molecular deformation behavior between those two types of silk. Figure 3 shows the Raman spectra of both silks upon uniaxial deformation in tension. While the native silk showed distinctive Raman band shifts to lower wavenumber (particularly, amide **I**, amide **III**, and ν(C−C) stretching), the Al-infiltrated silk showed less significant shifts. However, the peaks of amide **III** and ν(N−H) stretching modes of the Al-infiltrated silk exhibited noticeable peak shape changes, which implies that the main differences in the mechanical properties of both silks are most likely related to deformations of the β-sheet crystals and hydrogen bonds, which will be discussed in more detail later.

Upon uniaxial tension of the native silk, as shown in the plot of wavenumber versus strain (Figure 4a−c), the wavenumber associated with the ν(C−C) skeletal stretching showed an approximately linear shift to lower frequencies, in agreement with earlier findings.[23] In contrast, the Al-infiltrated spider silk showed a less-explicit relationship between wavenumber shift and strain. Similar trends were observed from the correlation of the wavenumber shifts with the applied stress. Figure 4d shows a redshift in the case of native silk, while a shift could not be clearly observed with the Al-infiltrated silk. The negligible dependence of the ν(C−C) skeletal stretching mode in the Al-infiltrated silk on stress and strain implied that the deformation mechanisms of both silks are rather different, as can be further speculated from the peak shifts observed in the amide **I** region.

Amide I Band. Previous theoretical studies suggested that the amide **I** band (dominantly C═O stretching) frequency is sensitive to the hydrogen bonding at the C═O group.[35] As shown in Figure 5, the native silk displayed a redshift with respect to both strain and stress, which in turn alluded that some bonds present in the β-sheet crystal regions, that is, (−C═O···H−N−C−), are likely to be weakened or broken (e.g., (−C═O, H−N−C−)) upon the applied stress or strain. In contrast, the wavenumber shift was observed to be almost

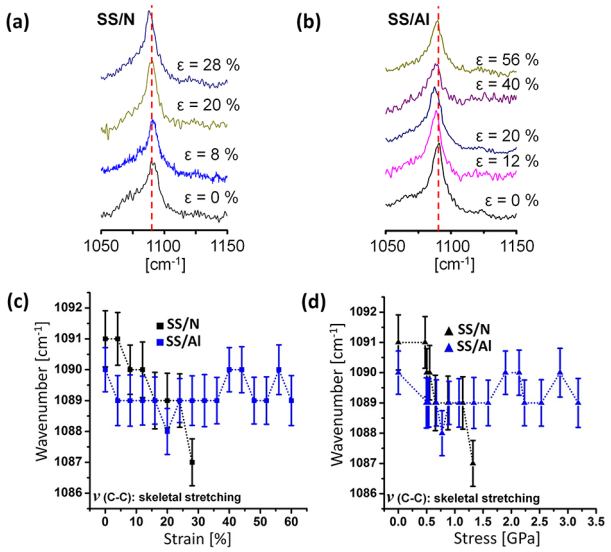

Figure 4. Comparison of Raman peak shifts of the ν(C−C) skeletal stretching mode with strain. (a) Native spider silk. (b) Al infiltrated spider silk. For the demonstration, representative Raman spectra of SS/N and SS/Al were selected, respectively. (c, d) Raman wavenumber shifts of the ν(C−C) stretching mode of SS/N and SS/Al with standard deviations plotted as a function of applied strain and stress, respectively.

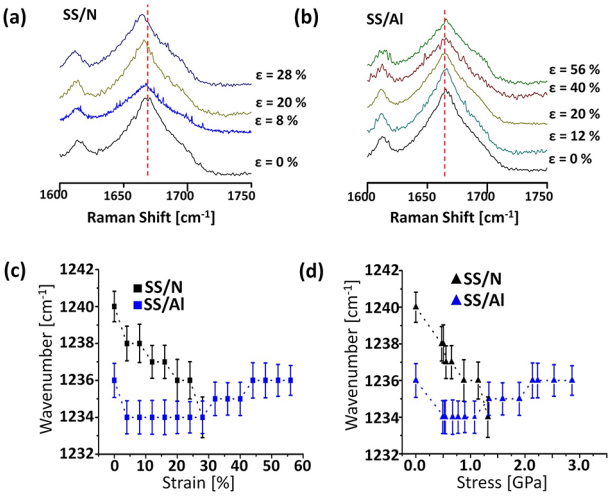

Figure 5. Comparison of Raman peak shifts of the ν(C═O) stretching mode (amide **I**) with strain. (a) Native spider silk. (b) Al-infiltrated spider silk. For the demonstration, representative Raman spectra of SS/N and SS/Al were selected, respectively. (c, d) Raman wavenumber shifts of the amide **I** mode of SS/N and SS/Al with standard deviations plotted as a function of the applied strain and stress, respectively.

independent of the stress and strain in the case of Al-infiltrated silk. Presumably the infiltrated Al interrupted some hydrogen bonds, and therefore some (−C═O) groups do not further participate in the hydrogen-bonding network. In contrast to the amide **I** band, the amide **III** band (ν(C−N)) contains dominantly coupling effects of the (C−N) stretching and (H−N−C) in plane bending modes. Thus, different behavior of the bands is expected. However, Figure 6 shows similarity to the earlier findings. The native silk displayed redshift under tension, whereas the Al-infiltrated silk showed less noticeable dependence. In analogy to the previously described case of the

dx.doi.org/10.1021/am5041797 | ACS Appl. Mater. Interfaces 2014, 6, 16827−16834

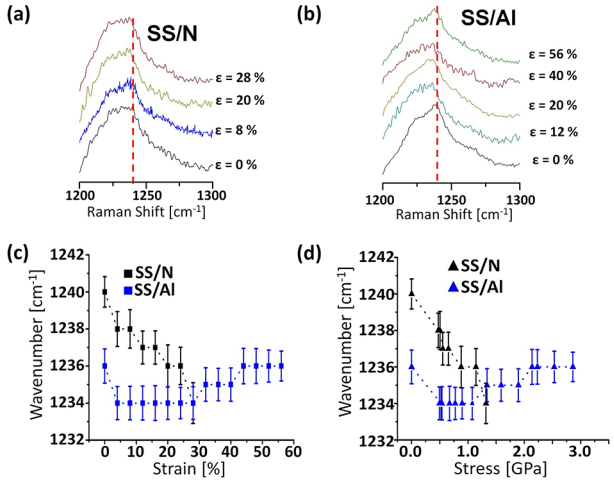

Figure 6. Comparison of Raman peak shifts of the ν(C−N) stretching mode (amide **III**) with strain. (a) Native spider silk. (b) Al-infiltrated spider silk. For the demonstration, representative Raman spectra of SS/N and SS/Al were selected, respectively. (c, d) Raman wavenumber shifts of the amide **III** mode of SS/N and SS/Al with standard deviations plotted as a function of applied strain and stress, respectively.

(−C═O) group in amide **I**, the stretching mode of the (H−N−C) groups of the Al-infiltrated silk shows a lower band shift than those of the native silk upon tension.

Amide III Band. Although Raman band shifts in the amide **III** region were observed to be less recognizable, the amide **III** band is known to reveal some information on the local stress within silk microstructures.[23] For further understanding we deconvoluted the amide **III** band region with four Lorentzian peaks and assigned Phy/Tyr, β-sheet, disordered random coil, and α-helix to the deconvoluted peaks (Figure 7a,b) referring to the procedures described in literature.[36−38] Yeh et al. reported that generally, in high-performance polymers, such as Kevlar and Twaron, the full width at half-maximum (fwhm) values of Raman bands significantly increase upon tensile

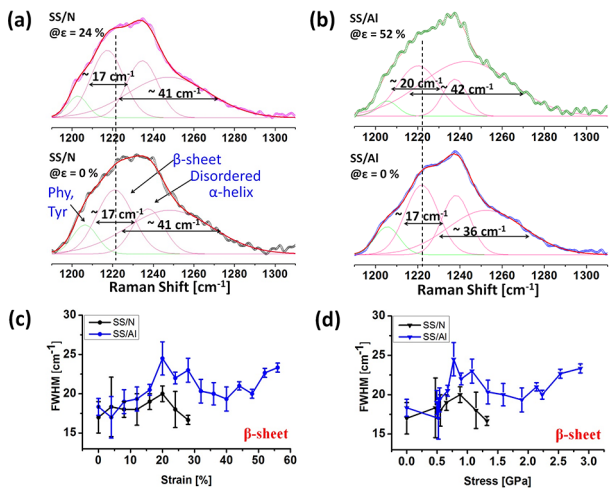

Figure 7. Comparison of deconvolution results of the amide **III** band. (a) SS/N at ε = 0 and ε = 24%. (b) SS/Al at ε = 0 and ε = 52%. For the demonstration, representative Raman spectra of SS/N and SS/Al were selected, respectively. (c, d) The fwhm values with standard deviations of peaks related to the β-sheet crystal as a function of strain and stress, respectively.

deformation.[39] They observed that the degree of molecular orientation and crystallinity in polymers is inversely proportional to the failure strain of the polymer and the variation of the fwhm in the Raman band. As rationale behind these phenomena, they suggested the high level of orientation and crystallinity, which results in a homogeneous stress distribution among the molecules during tensile deformation.[40] Figure 7c,d shows the variation of fwhm values in β-sheet crystals upon strain and stress, respectively. Compared to the native silk, the Al-infiltrated silk exhibits larger band broadening, being indicative for a lower fraction of crystalline/oriented microstructures. Taking further into account that failure strain of the silk was significantly increased after Al-infiltration and that less crystalline/oriented polymers generally show larger failure strain, the microstructure of the silk appears to be seriously altered by the Al-infiltration. In addition, it is highly likely that the hydrogen bonds are inextricably bound up with such Al-meditated microstructure changes of the silks, as can be deduced from the analysis of amide **A** region (Figure 8).

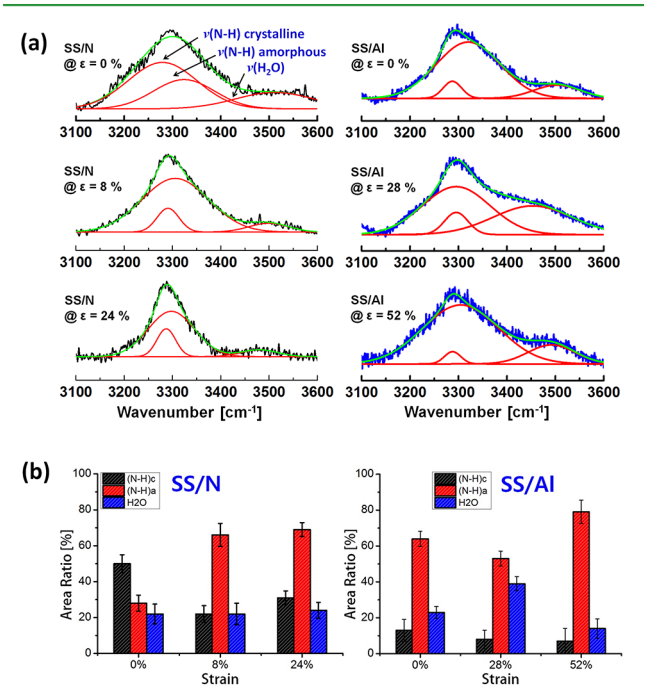

Figure 8. Evolution of the amide **A** (ν(N−H/H2O)) band in SS/N and SS/Al. (a) Variations of ν(N−H/H2O) bands with respect to applied strains and deconvolutions. For the demonstration, representative Raman spectra of SS/N and SS/Al were selected, respectively. (b) The relative areas of the different components in SS/N and SS/Al with standard deviations at applied strains, respectively (see text for details).

Amide A Band. The broad band near 3280 cm^{-1} is assigned to the amide **A** band, that is, ν(N−H) stretching of free and hydrogen-bonded amino acid residues within the protein's secondary structures (α-helix and β-sheet) of which the silk is comprised. The interchain hydrogen bonds are supposed to control the mechanical properties of the silk, for instance, rigidity (tension of the peptide chain) and elasticity (disentanglement of the chain in amorphous regions).[41] The ν(N−H) stretching mode in the hydrogen bonds is known to be used to probe the interchain distances.[42] Therefore, to take hints on the local microstructure changes of the silk, it is reasonable to monitor the variation of the ν(N−H) signatures.

dx.doi.org/10.1021/am5041797 | ACS Appl. Mater. Interfaces 2014, 6, 16827−16834

Generally, the intensity of the individual Raman peak depends on the number of molecules present (concentration). The change of concentration (e.g., dilution) can lead to peak broadening. Taking into account that the peak intensity can be severely changed by broadening, the integrated area of the peak is a better indicator of concentration because the area will remain unchanged once the total number of molecules is constant. Colomban et al. recently reported that the ν(N−H) mode in silk is composed of two bands, the first one assigned to the N−H vibrations in the crystalline macromolecular chains and the second one assigned to be those in the amorphous matrix.[43,44] They showed that through deconvolution of the ν(N−H) region using Lorentzian and Gaussian functions, the crystallinity of the silk can be estimated. In other words, from the areal ratio of the crystalline/amorphous band, the degree of the crystallinity can be determined. On the basis of these reports, we performed a deconvolution of the ν(N−H) region using one Lorentzian for the crystalline phase and one Gaussian for the amorphous phase, as shown in Figure 8a. As can be seen in Figure 8b, in the case of the native silk, before applying stress the crystalline band was observed to be stronger than the amorphous band. In contrast, the Al-infiltrated silk showed the opposite trend. It can be derived that the Al-infiltrated silk contains lower amounts of crystalline phase and a higher fraction of amorphous phase than the native silk. The native silk showed a tendency of the crystalline/amorphous fraction to visibly decrease/increase with strain, respectively. In contrast, the fraction change in the Al-infiltrated silk was less substantial although it showed similar tendency.

Changes in Microstructure of Silk after Al-Infiltration. As mentioned above, spider dragline silk is commonly described as a biopolymer containing two structural constituents, namely, β-sheet crystalline fractions and amorphous fractions, with protein chains in both cases being linked with hydrogen bonds. It has been widely accepted that the tensile strength and the extensibility of the spider dragline silk are mainly determined by both crystal size and their orientation.[25,45−47] Specifically, the size of the β-sheet crystals is inversely proportional to the tensile strength and directly proportional to the failure strain. Considering these facts and the observed variations in the Raman spectra, both the crystalline and amorphous regions of the dragline silk appear to be modified by the Al infiltration, so that the resulting Al-infiltrated silk shows pronounced improvements in both strength and extensibility. Taking into account the strong reactivity of the precursor molecules (TMA), the vaporized precursor molecules appear to diffuse into the bulk of the fibers.[48] Subsequently, the hydrogen bonds are likely to be converted into covalent bonds by chemical interaction of the vaporized precursor molecules with the protein backbone and parallel consumption of remaining bound water, which occurs both in crystalline and amorphous regions. In particular, in crystalline regions, those hydrogen bonds near the boundaries of the crystals would be eliminated first. In this way, crystalline parts are likely to be partially converted into supplemental amorphous regions. Accordingly, the amorphous fraction would increase, which is in agreement with the variation of the ν(N−H) band shown in Figure 8. As a result, the Al-infiltrated silk shows smaller β-sheet crystallites and more amorphous protein than those in the native silk. Indeed, our earlier wide-angle X-ray diffraction (WAXD) study on Ti-infiltrated *Araneus* spider dragline silk already revealed that the β-sheet crystals likely shrink after Ti infiltration.[13] The speculative mechanism explaining the changes of the protein structures inside the dragline silk by ALD are addressed in our earlier work.[13,19−21] The current Al-infiltrated *Nephila* spider silk also showed similar tendency. As can be recognized from WAXD results in Figure 9, the SS/Al showed the increase of the full width at

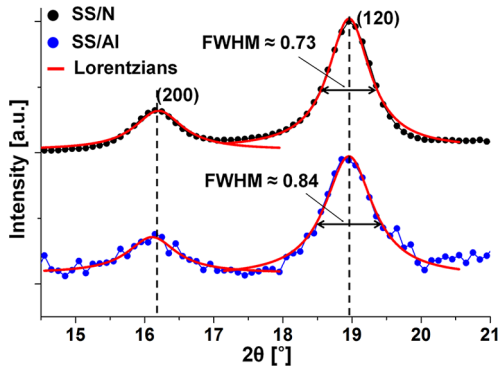

Figure 9. Wide angle X-ray diffraction result. On the basis of the report by Warwicker[49] and Marsh et al.,[50] the peaks are indexed as (120) and (200). Each peak was fitted with a Lorentzian function, from which the fwhm was estimated. In the peak (120), slight peak broadening was observed.

half-maximum (fwhm) of the main peak (120) assigned based on the report by Warwicker[49] and Marsh et al.[50] Such peak broadening is known to be generally caused by reduction of crystallite size or lattice distortion inside the crystallites.[51,52] Considering the current results from Raman spectra and WAXD, it is highly probable that the sizes of the β-sheet crystallites are reduced by Al infiltration. It was notable that the main peak of the *Nephila* spider silk is located on higher angle ($2\theta \approx 19°$) than the *Araneus* spider silk ($2\theta \approx 17°$).[13] It means that the β-sheet crystallite of the *Nephila* silk is smaller than that of the *Araneus* silk. Considering the report that the former has higher failure strain than the latter,[22] it is highly probable that the smaller the crystal size is, the higher the extensibility.

Molecular Deformation Behavior of Al-Infiltrated Silk upon Tension. On the basis of the relative comparison of Raman-band shifts in the native and Al-infiltrated silk (i.e., ν(C−C), ν(C═O), ν(C−N), and ν(N−H)) observed during tensile deformation, the deformation behavior of those two silks could be approximately described, although other analyses are still needed for more detailed description. As mentioned previously, the microstructure of the silk is known to be largely composed of stiff β-sheet crystals embedded in a soft amorphous matrix. Upon deformation, both crystallites and amorphous constituents of the silk fiber are subjected to uniform stress. In contrast, because of the different moduli of crystalline and amorphous regions, the strain is not uniform.[22] Recent studies reported on the role of β-sheet crystal and its size effects on the strength and toughness of the dragline silk within a theoretical framework.[45−47] The studies also addressed the expected molecular deformation behavior of the silk under tension. The proposed deformation mechanism related to the size effect of the β-sheet crystal can also be applied to our Al-infiltrated silk with a reduced crystal size. In the case of the native dragline silk, as well described in the study by Nova et al.[46] and roughly depicted in Figure 10a, upon initial stretching, the amorphous regions are homogeneously aligned with the silk axis without breaking the hydrogen bonds until yielding occurs (region **I** in Figure 1a). Subsequently, the hydrogen bonds in

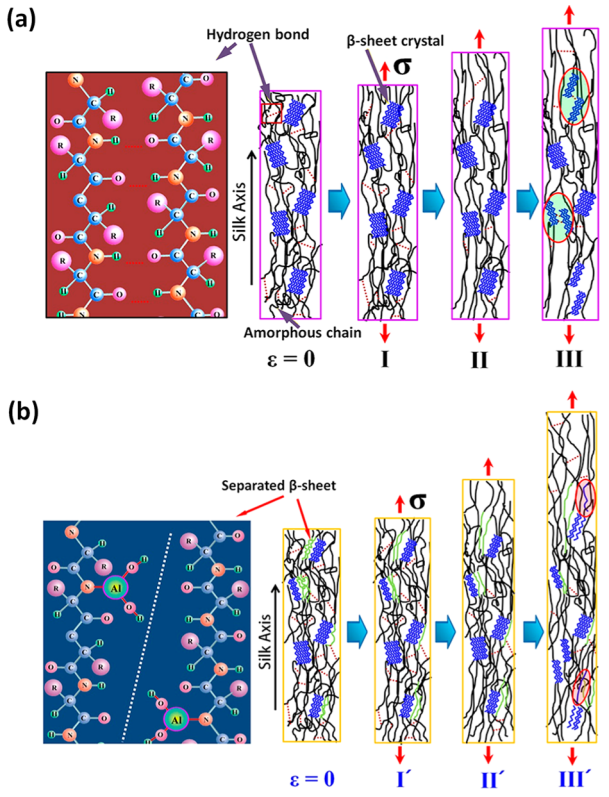

Figure 10. Hypothesized models depicting molecular deformation behaviors with strain of (a) SS/N and (b) SS/Al (see text for details).

the amorphous fraction presumably start to rupture. Subsequently, the polypeptide chain gradually unravels as the hydrogen bonds continue breaking. The hidden polypeptide length allows the silk to experience low stress values despite the increasing strain values, which is likely observed as a plateau region in the stress–strain curve (region **II** in Figure 1a). After the amorphous chains are fully stretched, the hydrogen bond rupture proceeds from amorphous to β-sheet crystallized polypeptides. The crystals have higher stiffness and sustain higher stress and larger strain (region **III** in Figure 1a) before reaching the point of failure. The region **III** determines the overall breaking energy (toughness) of the silk, which is closely related to the size of the β-sheet crystals. More specifically, it has been reported that smaller β-sheet crystals are primarily subjected to uniform shear force under tension, which allows cooperative rupture of interchain hydrogen bonds and a stick–slip energy dissipation mechanism. Hence, once the individual β-sheets are nearly completely stretched, failure occurs (red colored circle in Figure 10b). In contrast, as predicted by Keten et al.,[47] larger crystals undergo nonuniform shear force of interchain hydrogen bonds under tension, which leads to cracklike flaw formation, and consequently, they fail catastrophically (green colored circle in Figure 10a). For this reason, smaller crystals provide greater stiffness, fracture toughness, and extensibility in comparison to larger crystals. Indeed, as can be recognized from the stress–strain curve in Figure 1a, the Al-infiltrated silk shows greater toughness and much higher extensibility than the native silk likely owing to a smaller size of the β-sheet crystals. The substantial increase in the extensibility can also be largely attributed to the newly created amorphous polypeptides by the Al-infiltration (Figure 10b), as can be deduced from the comparison between regions **III** and **III′** marked in the stress–strain curve (Figure 1a).

CONCLUSIONS

In summary, motivated by natural metal-impregnated biological materials with amazing physical properties, we have produced an Al-infiltrated dragline silk of *Nephila pilipes* spider. The resulting dragline silk has shown impressively increased strength and extensibility as compared to the native dragline silk. In situ Raman spectroscopic studies provided comparative information on the tensile deformation behavior of both native and infiltrated silk at the molecular level. From the Raman spectra and WAXD results of both silks, we were able to learn that the molecular structure changes upon Al infiltration presumably occur at the hydrogen-bonding sites, which is likely to result in covalent bond formation between Al ions and amino acids and consequential size reductions of the β-sheet crystals. The observation of Raman shifts with increasing strain has revealed that not only the strength but also the extensibility of the silk are dominantly governed by the size of the β-sheet crystals.

AUTHOR INFORMATION

Corresponding Author

*E-mail: sm.lee@kimm.re.kr.

Notes

The authors declare no competing financial interest.

ACKNOWLEDGMENTS

This research was supported by the Development Program of Manufacturing Technology for Flexible Electronics with High Performance (SC0970) and Innovative Research Programs (KM3220) funded by of Korea Institute of Machinery and Materials (KIMM). M.K. greatly acknowledges financial support by the Spanish ministry of economy and competitivity (MINECO) through project number MAT2012-38161 and the Basque government through project number PI2013-56.

REFERENCES

(1) Edwards, M. Genghis Khan. *National Geographic* **1996**, No. December, 2–37.
(2) Turnbull, S. *Mongol Warrior 1200–1350;* Osprey Publishing: Oxford, 2003.
(3) Vollrath, F.; Knight, D. P. Liquid Crystalline Spinning of Spider Silk. *Nature* **2001**, *410*, 541–548.
(4) Gosline, J. M.; Guerette, P. A.; Ortlepp, C. S.; Savage, K. N. The Mechanical Design of Spider Silk: From Fibroin Sequence to Mechanical Function. *J. Exp. Biol.* **1999**, *202*, 3295–3303.
(5) Gosline, J. M.; DeMont, M. E.; Denny, M. W. The Structure and Properties of Spider Silk. *Endeavour* **1987**, *10*, 37–43.
(6) Scheibel, T. Spider Silks: Recombinant Synthesis, Assembly, Spinning, and Engineering of Synthetic Protein. *Microb. Cell Fact.* **2004**, *3*, 14.
(7) Lazaris, A.; Arcidiacono, S.; Huang, Y.; Zhou, J.-F.; Duguay, F.; Chretien, N.; Welsh, E. A.; Soares, J. W.; Karatzas, C. N. Spider Silk Fibers Spun from Soluble Recombinant Silk Produced in Mammalian Cells. *Science* **2002**, *295*, 472–476.
(8) Dunaway, D. L.; Thiel, B. L.; Viney, C. Tensile Mechanical Property Evaluation of Natural and Epoxide-Treated Silk Fibers. *J. Appl. Polym. Sci.* **1995**, *58*, 675–683.
(9) Mayes, E. L.; Vollrath, F.; Mann, S. Fabrication of Magnetic Spider Silk and Other Silk-Fiber Composites Using Inorganic Nanoparticles. *Adv. Mater.* **1998**, *10*, 801–805.

(10) Ayutsede, J.; Gandhi, M.; Sukigara, S.; Ye, H.; Hsu, C.; Gogotsi, Y.; Ko, F. Carbon Nanotube Reinforced Bombyx mori Silk Nanofibers by the Electrospinning Process. *Biomacromolecules* **2006**, *7*, 208−214.
(11) Kim, H.; Che, L.; Ha, Y.; Ryu, W. Mechanically-reinforced Electrospun Composite Silk Fibroin Nanofibers Containing Hydroxyapatite Nanoparticles. *Mater. Sci. Eng., C* **2014**, *40*, 324−335.
(12) Saravanan, D. Spider Silk-Structure, Properties and Spinning. *J. Text. Apparel Technol. Manage.* **2006**, *5*, 1−20.
(13) Lee, S.-M.; Pippel, E.; Gösele, U.; Dresbach, C.; Qin, Y.; Chandran, C. V.; Bräuniger, T.; Hause, G.; Knez, M. Greatly Increased Toughness of Infiltrated Spider Silk. *Science* **2009**, *324*, 488−492.
(14) Broomell, C. C.; Mattoni, M. A.; Zok, F. W.; Waite, J. H. Critical Role of Zinc in Hardening of *Nereis* Jaws. *J. Exp. Biol.* **2006**, *209*, 3219−3225.
(15) Werneke, S. W.; Swann, C.; Farquharson, L. A.; Hamilton, K. S.; Smith, A. M. The Role of Metals in Molluscan Adhesive Gels. *J. Exp. Biol.* **2007**, *210*, 2137−2145.
(16) Vaccaro, E.; Waite, J. H. Yield and Post-Yield Behavior of Mussel Byssal Thread: A Self-Healing Biomolecular Material. *Biomacromolecules* **2001**, *2*, 906−911.
(17) Chiovitti, A.; Heraud, P.; Dugdale, T. M.; Hodson, O. M.; Curtain, R. C. A.; Dagastine, R. R.; Wood, B. R.; Wetherbee, R. Divalent Cations Stabilize the Aggregation of Sulfated Glycoproteins in the Adhesive Nanofibers of the Biofouling Diatom *Toxarium undulatum*. *Soft Matter* **2008**, *4*, 811−820.
(18) Lee, S.-M.; Grass, G.; Kim, G.-M.; Dresbach, C.; Zhang, L.; Gösele, U.; Knez, M. Low-Temperature ZnO Atomic Layer Deposition on Biotemplates: Flexible Photocatalytic ZnO Structures from Eggshell Membranes. *Phys. Chem. Chem. Phys.* **2009**, *11*, 3608−3614.
(19) Lee, S.-M.; Pippel, E.; Moutanabbir, O.; Gunkel, I.; Thurn-Albrecht, T.; Knez, M. Improved Mechanical Stability of Dried Collagen after Metal Infiltration. *ACS Appl. Mater. Interfaces* **2010**, *2*, 2436−2441.
(20) Lee, S.-M.; Pippel, E.; Knez, M. Metal Infiltration into Biomaterials by ALD and CVD: A Comparative Study. *ChemPhysChem* **2011**, *12*, 791−798.
(21) Lee, S.-M.; Ischenko, V.; Pippel, E.; Masic, A.; Moutanabbir, O.; Fratzl, P.; Knez, M. An Alternative Route towards Metal-Polymer Hybrid Materials Prepared by Vapor Phase Processing. *Adv. Funct. Mater.* **2011**, *21*, 3047−3055.
(22) Stauffer, S. L.; Coguill, S. L.; Lewis, R. V. Comparison of Physical Properties of Three Silks from *Nephila clavipes* and *Araneus* gemmoides. *J. Arachnol.* **1994**, *22*, 5−11.
(23) Sirichaisit, J.; Brookes, V. L.; Young, R. J.; Vollrath, F. Analysis of Structure/Property Relationships in Silkworm (*Bombyx mori*) and Sider Dragline (*Nephila edulis*) Silks Using Raman Spectroscopy. *Biomacromolecules* **2003**, *4*, 387−394.
(24) Work, R. W.; Emerson, P. D. An Apparatus and Technique for the Forcible Silking of Spiders. *J. Arachnol.* **1982**, *10*, 1−10.
(25) Du, N.; Liu, X. Y.; Narayanan, J.; Li, L.; Lim, M. L. M.; Li, D. Design of Superior Spider Silk: from Nanostructure to Mechanical Properties. *Biophys. J.* **2006**, *91*, 4528−4535.
(26) Miller, D. C.; Foster, R. R.; Jen, S. H.; Bertrand, J. A.; Cunningham, S. J.; Morris, A. S.; Lee, Y. C.; George, S. M.; Dunn, M. L. Thermo-Mechanical Properties of Alumina Films Created Using the Atomic Layer Deposition Technique. *Sens. Actuators, A* **2010**, *164*, 58−67.
(27) Lin, L. H.; Edmonds, D. T.; Vollrath, F. Structural Engineering of an Orb-Spider's Web. *Nature* **1995**, *373*, 146−148.
(28) Jen, S.-H.; George, S. M. Alucone Interlayers to Minimize Stress Caused by Thermal Expansion Mismatch between Al_2O_3 Films and Teflon Substrates. *ACS Appl. Mater. Interfaces* **2013**, *5*, 1165−1173.
(29) Hinman, M. B.; Lewis, R. V. Isolation of a Clone Encoding a Second Dragline Silk Fibroin. *Nephila clavipes* Dragline Silk is a Two-Protein Fiber. *J. Biol. Chem.* **1992**, *267*, 19320−19324.
(30) Simmons, A. H.; Michal, C. A.; Jelinski, L. W. Molecular Orientation and Two-Component Nature of the Crystalline Fraction of Spider Dragline Silk. *Science* **1996**, *271*, 84−87.
(31) van Beek, J. D.; Hess, S.; Vollrath, F.; Meier, B. H. The Molecular Structure of Spider Dragline Silk: Folding and Orientation of the Protein Backbone. *Proc. Natl. Acad. Sci. U.S.A.* **2002**, *99*, 10266−10271.
(32) Work, R. W.; Young, C. T. The Amino Acid Compositions of Major and Minor Ampullate Silks of Certain Orb-Web-Building Spiders (*Araneae, Araneidea*). *J. Arachnol.* **1987**, *15*, 65−80.
(33) Colomban, P.; Hung, M. D.; Riand, J.; Prinsloo, L. C.; Mauchamp, B. Nanomechanics of Single Silkworm and Spider Fibres: A Raman and Micro-mechanical in situ Study of the Conformation Change with Stress. *J. Raman Spectrosc.* **2008**, *39*, 1749−1764.
(34) Edwards, H. G. M.; Farwell, D. W. Raman Spectroscopic Studies of Silk. *J. Raman Spectrosc.* **1993**, *26*, 901−909.
(35) Myshakina, N. S.; Zeeshan, A.; Asher, S. A. Dependence of Amide Vibrations on Hydrogen Bonding. *J. Phys. Chem. B* **2008**, *112*, 11873−11877.
(36) Tsukada, M.; Freddi, G.; Monti, P.; Bertoluzza, A.; Kasai, N. Structure and Molecular Conformation of Tussah Silk Fibroin Films: Effect of Methanol. *J. Polym. Sci., Part B: Polym. Phys.* **2003**, *33*, 1995−2001.
(37) Ling, S.; Qi, Z.; Knight, D. P.; Shao, Z.; Chen, X. Synchrotron FTIR Microspectroscopy of Single Natural Silk Fibers. *Biomacromolecules* **2011**, *12*, 3344−3349.
(38) Lefèvre, T.; Boudreault, S.; Cloutier, C.; Pézolet, M. Diversity of Molecular Transformations Involved in the Formation of Spider Silks. *J. Mol. Biol.* **2011**, *405*, 238−253.
(39) Yeh, W.-Y.; Young, R. J. Molecular Deformation Processes in Aromatic High Modulus Polymer Fibres. *Polymer* **1999**, *40*, 857−870.
(40) Yeh, W.-Y.; Young, R. J. Deformation Processes in Poly(ethylene terephthalate) Fibers. *J. Macromol. Sci., Part B: Phys.* **1998**, *B37*, 83−118.
(41) Colomban, P.; Gouadec, G. Raman and IR Micro-analysis of High Performance Polymer Fibres Tested in Traction and Compression. *Compos. Sci. Technol.* **2009**, *69*, 10−16.
(42) Novak, A. Hydrogen Bonding in Solids. Correlation of Spectroscopic and Crystallographic Data. *Struct. Bonding (Berlin, Ger.)* **1974**, *18*, 177−216.
(43) Colomban, P. Understanding the Nano- and Macromechanical Behaviour, the Failure and Fatigue Mechanisms of Advanced and Natural Polymer Fibres by Raman/IR Microspectrometry. *Adv. Nat. Sci.: Nanosci. Nanotechnol.* **2013**, *4*, 013001.
(44) Colomban, P.; Dinh, H. M. Origin of the Variability of the Mechanical Properties of Silk Fibres: 2 The Nanomechanics of Single Silkworm and Spider Fibres. *J. Raman Spectrosc.* **2012**, *43*, 1035−1041.
(45) Termonia, Y. Molecular Modeling of Spider Silk Elasticity. *Macromolecules* **1994**, *27*, 7378−7381.
(46) Nova, A.; Keten, S.; Pugno, N. M.; Redaelli, A.; Buehler, M. J. Molecular and Nanostructural Mechanisms of Deformation, Strength and Toughness of Spider Silk Fibrils. *Nano Lett.* **2010**, *10*, 2626−2634.
(47) Keten, S.; Xu, Z.; Ihle, B.; Buehler, M. J. Nanoconfinement Controls Stiffness, Strength and Mechanical Toughness of β-sheet Crystals in Silk. *Nat. Mater.* **2010**, *9*, 359−367.
(48) Wilson, C. A.; Grubbs, R. K.; George, S. M. Nucleation and Growth during Al_2O_3 Atomic Layer Deposition on Polymers. *Chem. Mater.* **2005**, *17*, 5625−5634.
(49) Warwicker, J. O. Comparative Studies of Fibrous. II. The Crystal Structure of Various Fibroins. *J. Mol. Biol.* **1960**, *2*, 350−362.
(50) Marsh, R. E.; Corey, R. B.; Pauling, L. An Investigation of the Structure of Silk Fibroin. *Biochim. Biophys. Acta* **1955**, *16*, 1−34.
(51) Guinier, A. *X-ray Diffraction in Crystals, Imperfect Crystals, and Amorphous Bodies;* Dover: New York, 1994.
(52) Grubb, D. T.; Jelinski, L. W. Fiber Morphology of Spider Silk: the Effect of Tensile Deformation. *Macromolecules* **1997**, *30*, 2860−2867.